Accumulation of heavy particles around a helical vortex filament

Rutger H. A. IJzermans, Rob Hagmeijer, and Pieter J. van Langen
Department of Mechanical Engineering, University of Twente, P.O. Box 217, 7500 AE Enschede, The Netherlands

(Received 29 November 2006; accepted 5 June 2007; published online 5 October 2007)

The motion of small heavy particles near a helical vortex filament in incompressible flow is investigated. Both the configurations of a helical vortex filament in free space and a helical vortex filament in a concentric pipe are considered, and the corresponding helically symmetric velocity fields are expressed in terms of a stream function. Particle motion is assumed to be driven by Stokes drag, and the flow fields are assumed to be independent from the motion of particles. Numerical results show that heavy particles may be attracted to helical trajectories. The stability of these attraction trajectories is demonstrated by linear stability analysis. In addition, the correlation between the attraction trajectories and the streamline topologies is investigated. © *2007 American Institute of Physics*. [DOI: 10.1063/1.2771658]

I. INTRODUCTION

Helical vortex filaments are observed in many natural and industrial applications.[1] They can be found in wakes downstream of propellers and wind turbines,[2] in combustive flows containing a precessing vortex core,[3] and in industrial gas conditioners used for the separation of heavy particles and droplets.[4,5] In addition, a recent numerical study has shown that the advection of fluid particles in turbulence is largely influenced by the presence of small-scale helical vortices.[6] Helical vortex structures are also interesting from a theoretical point of view, because a helical vortex filament is the simplest three-dimensional vortex structure having nonzero curvature and nonzero torsion.[7–10] Although the flow field induced by a helical vortex filament has been widely studied, the motion of heavy particles in such flows has received relatively little attention. In the present paper, we present particle trajectories and attraction trajectories generated by helical vortex flow, both in free space as well as in a concentric pipe.

The velocity field induced by a vortex filament in an incompressible, inviscid fluid in free space is described by the Biot-Savart law. Hardin[11] evaluated the Biot-Savart law for the case of an infinite helical vortex filament in terms of an infinite series of modified Bessel functions. The same series had already been found by Lamb[12] when he calculated the magnetic field induced by a spool. The velocity field derived by Hardin is invariant along helical curves and may therefore be formulated in terms of a two-dimensional stream function in helical coordinates. Mezić *et al.*[13] showed that the resulting flow field can have three different topologies, depending on the values of the helix curvature, the helix pitch (the length of one revolution), and the thickness of the vortex core.

The flow field induced by a helical vortex filament in a concentric pipe is different from the free space configuration, since the radial velocity on the pipe wall is required to be zero. To approximately accommodate this boundary condition, Sarasúa *et al.*[14] employed a single image vortex of helical shape exterior to the pipe, which leads to an exact formulation in the limit of infinite pitch. Okulov[15] produces an exact formulation by rigorous solution of the governing partial differential equation. As an alternative, we derive the stream function by employing a vortex distribution on the pipe wall, which efficiently reproduces the result of Okulov.

From experiments and numerical studies,[3] it is known that a free helical vortex filament in a pipe can have a stationary shape, although the helix may propagate in itself. The self-induced velocity of a helical vortex filament can be calculated directly from the Biot-Savart law (see, e.g., Ref. 16), leading to a logarithmic term which is singular in the limit of zero-thickness of the vortex core. In reality the self-induced velocity is finite, and several models have been developed in order to overcome the singularity, see Refs. 17 and 18 for reviews. In the present work, the self-induced and wall-induced velocities are compensated for by a uniform axial velocity field, to obtain a stationary helix.

The motion of heavy particles has been investigated extensively in the last two decades. Early studies,[19,20] reveal inertial particles to distribute nonuniformly, which is generally referred to as preferential concentration. In general, heavy particles are ejected from regions of high vorticity, and accumulated in regions of high strain.[21] In some flow fields, initially uniformly distributed heavy particles tend to accumulate in attraction points. Particular examples of such flow fields are two-dimensional mixing layers,[22] rotating flows with a prescribed vorticity distribution,[23] and a three-dimensional Burgers vortex.[24] Recently, heavy particles have been shown to accumulate in a flow generated by an eccentric point vortex on a disk,[4] which corresponds to a helical vortex filament in a pipe in the limit of infinite pitch.[25]

In the present paper, we investigate the motion of heavy particles in the three-dimensional flow field around an infinite helical vortex filament, with the particle motion driven by Stokes drag. Gravity is neglected. Both the configuration of a helical vortex filament in a pipe and in free space are studied. It is shown that heavy particles are attracted to a helical trajectory. The attraction is shown to take place for a wide range of particle Stokes numbers, and to be closely

related to the streamline topology of the carrier flow. The results may be useful in the study of separation of heavy particles or droplets from gas flows, and for the clustering of fuel droplets in combustive flows with a precessing vortex core.

In Sec. II, we present the equations for the velocity field induced by a helical vortex filament in a concentric pipe. In addition, the equations for particle motion are presented and transformed to a helical frame of reference. Finally, the numerical integration method is outlined. In Sec. III, the streamline topologies encountered are identified, and Sec. IV presents the results for the motion of heavy particles. We identify attraction trajectories, and we demonstrate their stability by linear stability analysis. Finally, conclusions are formulated in Sec. V.

II. PHYSICAL-MATHEMATICAL MODEL

A. Flow field

We consider an infinitely long helical vortex filament with strength Γ, winding radius a, and pitch $h=2\pi l$, located within a cylindrical pipe with radius R. A uniform flow U_∞ in the axial direction is superimposed onto the flow field in order to fix the helix in space. All variables are made dimensionless by Γ and a, such that the problem is completely defined by the dimensionless parameters l/a, $U_\infty a/\Gamma$, and R/a. A sketch of the helix configuration is given in Fig. 1. It is noted that the case of a helical vortex filament in free space corresponds to the limit $R/a\to\infty$.

First, we define a helical curve, or helix, with pitch $2\pi l/a$, and dimensionless winding radius r as

$$\boldsymbol{h}\left(\alpha;\frac{l}{a},r,\alpha_0\right)=\left(r\cos(\alpha),r\sin(\alpha),(\alpha-\alpha_0)\frac{l}{a}\right)^T, \tag{1}$$

where α is the coordinate along the helix, and α_0 is the value of α for which the z coordinate is zero. Without loss of generality we choose the helical vortex filament as $\boldsymbol{h}(\alpha;l/a,1,0)$. The local tangent, normal, and binormal unit vectors (Frenet vectors) on helical curves are defined as

$$\boldsymbol{t}\equiv\frac{d\boldsymbol{h}}{d\alpha}\left\|\frac{d\boldsymbol{h}}{d\alpha}\right\|^{-1},\quad \boldsymbol{n}\equiv\frac{d^2\boldsymbol{h}}{d\alpha^2}\left\|\frac{d^2\boldsymbol{h}}{d\alpha^2}\right\|^{-1},\quad \boldsymbol{b}\equiv\boldsymbol{t}\times\boldsymbol{n}. \tag{2}$$

In terms of the unit basis vectors in cylindrical coordinates, $\boldsymbol{e}_r$, $\boldsymbol{e}_\theta$, and $\boldsymbol{e}_z$, and by introduction of

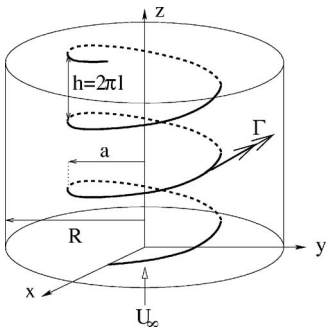

FIG. 1. Problem configuration for a helical vortex filament concentrically positioned in a pipe.

$$\beta\equiv\sqrt{1+\left(\frac{ar}{l}\right)^2}, \tag{3}$$

these expressions can be written as

$$\boldsymbol{t}=\beta\left(\boldsymbol{e}_z+\frac{ar}{l}\boldsymbol{e}_\theta\right),\quad \boldsymbol{n}=-\boldsymbol{e}_r,\quad \boldsymbol{b}=\beta\left(\frac{ar}{l}\boldsymbol{e}_z-\boldsymbol{e}_\theta\right). \tag{4}$$

To introduce the concept of helical symmetry, we use an orthogonal map $\boldsymbol{\xi}(\boldsymbol{x})$, which defines helical coordinates $\boldsymbol{\xi}=(\xi,\eta,\zeta)^T$ as

$$\boldsymbol{\xi}(\boldsymbol{x})=R\left(\frac{az}{l}\right)\boldsymbol{x},$$
$$R\left(\frac{az}{l}\right)=\begin{pmatrix}\cos\left(\frac{az}{l}\right) & \sin\left(\frac{az}{l}\right) & 0\\ -\sin\left(\frac{az}{l}\right) & \cos\left(\frac{az}{l}\right) & 0\\ 0 & 0 & 1\end{pmatrix}. \tag{5}$$

The map $\boldsymbol{\xi}(\boldsymbol{x})$ is illustrated in Fig. 2. Helical curves in the $\boldsymbol{x}$-frame reduce to straight lines parallel to the ζ-axis in the $\boldsymbol{\xi}$-frame. As a consequence, the helical vortex filament, which is projected onto the (x,y)-plane as the unit circle, is projected onto the (ξ,η)-plane as a single point. A function $f(\boldsymbol{x})$ is called helically symmetric if it is independent of ζ:

$$\frac{\partial f}{\partial\zeta}=0. \tag{6}$$

Let the velocity field in the $\boldsymbol{x}$-frame be denoted by $\boldsymbol{u}$. In terms of cylindrical coordinates related to the $\boldsymbol{x}$-frame, $(r,\theta,z)^T$, the velocity components are u_r, u_θ, and u_z, respectively. Furthermore, let the velocity field in the $\boldsymbol{\xi}$-frame be denoted by $\boldsymbol{v}$. In terms of cylindrical coordinates related to the $\boldsymbol{\xi}$-frame, $(r,\phi,\zeta)^T$ with $\phi\equiv\theta-za/l$, the velocity components are v_r, v_ϕ, and v_ζ, respectively. Then we have the following relations:[11]

$$v_r=u_r,\quad v_\phi=u_\theta-\frac{ar}{l}u_z,\quad v_\zeta=u_z. \tag{7}$$

For a helical vortex filament in free space, as well as for a helical vortex filament enclosed by a concentric circular

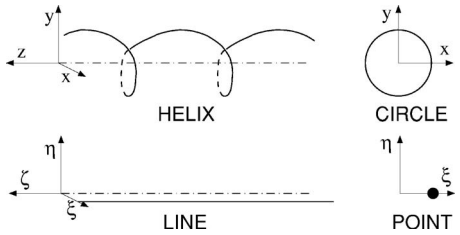

FIG. 2. Helical vortex filament in the $\boldsymbol{x}$-frame and in the $\boldsymbol{\xi}$-frame.

pipe, we have

$$\frac{\partial \boldsymbol{v}}{\partial \zeta} = 0, \tag{8}$$

i.e., the velocity field $\boldsymbol{v}$ is helically symmetric.[3,26]

Because of helical symmetry, the flow field can be described by a stream function $\Psi(r,\phi)$, and the velocities follow from the canonical equations

$$v_r = \frac{1}{r}\frac{\partial \Psi}{\partial \phi}, \quad v_\phi = -\frac{\partial \Psi}{\partial r}. \tag{9}$$

By taking into account the contribution due to the vortex filament itself, the contribution due to a vortex distribution on the pipe wall, and the contribution due to a uniform velocity in the axial direction, the stream function can be determined by the method presented in Appendix A. The result is

$$\Psi = \begin{cases} \dfrac{r^2a^2}{4\pi l^2} + \dfrac{r^2 a}{2l}\left(\dfrac{U_\infty a}{\Gamma}\right) - \dfrac{ra^2}{\pi l^2}\displaystyle\sum_{m=1}^{\infty} I_m'(mra/l)Z_m'(ma/l)\cos m\phi, & r<1, \\ \dfrac{a^2}{4\pi l^2} - \dfrac{1}{4\pi}\ln r^2 + \dfrac{r^2 a}{2l}\left(\dfrac{U_\infty a}{\Gamma}\right) - \dfrac{ra^2}{\pi l^2}\displaystyle\sum_{m=1}^{\infty} I_m'(ma/l)Z_m'(mra/l)\cos m\phi, & r>1, \end{cases} \tag{10}$$

with Z_m defined as

$$Z_m(mx/l) \equiv K_m(mx/l) - \frac{K_m'(mR/l)}{I_m'(mR/l)} I_m(mx/l). \tag{11}$$

Here, I_m and K_m denote modified Bessel functions of the first and second kind, respectively, and the prime represents differentiation with respect to the argument. It is noted that in the limit of $R/a \to \infty$, the function Z_m reduces to K_m, so that the free space formulation of Hardin[11] is retrieved.

The velocity components $(u_r, u_\theta, u_z)^T$ can be retrieved from Eq. (10) by using the vorticity $\boldsymbol{\omega} = \nabla \times \boldsymbol{u}$. Since $\boldsymbol{\omega}\cdot\boldsymbol{n} = 0$ and $\boldsymbol{\omega}\cdot\boldsymbol{b} = 0$ everywhere in the flow, it can be shown by using Eq. (4) that

$$u_z + r\frac{a}{l}u_\theta = u_0, \tag{12}$$

where u_0 is a constant. By means of Eqs. (7) and (12), we can express the three components of $\boldsymbol{u}$ in terms of v_r, v_ϕ, and u_0,

$$u_r = v_r, \quad u_\theta = \beta^2\left(v_\phi + r\frac{a}{l}u_0\right), \quad u_z = \beta^2\left(u_0 - r\frac{a}{l}v_\phi\right). \tag{13}$$

The value of u_0 can be determined by noting that $\boldsymbol{\omega}\cdot\boldsymbol{t} = 0$ everywhere except at the vortex filament,

$$\boldsymbol{\omega}\cdot\boldsymbol{t} = \frac{2\beta^5 u_0 a}{l} - \beta\left[\frac{1}{r^2}\frac{\partial^2\Psi}{\partial\phi^2} + \frac{1}{r}\frac{\partial}{\partial r}\left(r\beta^2\frac{\partial\Psi}{\partial r}\right)\right] = 0, \quad \forall\ (r,\phi) \neq (1,0), \tag{14}$$

which leads to

$$u_0 = \frac{a}{2\pi l} + \frac{U_\infty a}{\Gamma}. \tag{15}$$

As a result, the velocity components $(u_r, u_\theta, u_z)^T$ become

$$u_r = \begin{cases} \dfrac{a^2}{\pi l^2}\displaystyle\sum_{m=1}^{\infty} mI_m'\left(\frac{ma}{l}r\right)Z_m'\left(\frac{ma}{l}\right)\sin m\phi, & r<1, \\ \dfrac{a^2}{\pi l^2}\displaystyle\sum_{m=1}^{\infty} mI_m'\left(\frac{ma}{l}\right)Z_m'\left(\frac{ma}{l}r\right)\sin m\phi, & 1<r<\dfrac{R}{a}, \end{cases} \tag{16}$$

$$u_\theta = \begin{cases} \dfrac{a}{\pi r l}\displaystyle\sum_{m=1}^{\infty} mI_m\left(\frac{ma}{l}r\right)Z_m'\left(\frac{ma}{l}\right)\cos m\phi, & r<1, \\ \dfrac{1}{2\pi r} + \dfrac{a}{\pi r l}\displaystyle\sum_{m=1}^{\infty} mI_m'\left(\frac{ma}{l}\right)Z_m\left(\frac{ma}{l}r\right)\cos m\phi, & 1<r<\dfrac{R}{a}, \end{cases} \tag{17}$$

$$u_z = \begin{cases} \dfrac{U_\infty a}{\Gamma} + \dfrac{a}{2\pi l} - \dfrac{a^2}{\pi l^2}\displaystyle\sum_{m=1}^{\infty} m I_m\left(\frac{ma}{l}r\right) Z'_m\left(\frac{ma}{l}\right)\cos m\phi, & r<1, \\ \dfrac{U_\infty a}{\Gamma} - \dfrac{a^2}{\pi l^2}\displaystyle\sum_{m=1}^{\infty} m I'_m\left(\frac{ma}{l}\right) Z_m\left(\frac{ma}{l}r\right)\cos m\phi, & 1<r<\dfrac{R}{a}. \end{cases} \tag{18}$$

Equations (16)–(18) are identical to the results obtained by Alekseenko *et al.*[3]

B. Particle motion

In many applications, such as gas-liquid separators, the particle-laden flow is dilute, and one-way coupling is an adequate approximation. In the present paper the particles are assumed to be small, spherical, and to have a much higher mass density than the carrier flow. Finally, gravity is neglected. Under these conditions, the dimensionless equations of motion for the particles, established by Maxey and Riley,[27] reduce to

$$\frac{d\boldsymbol{x}^p}{dt} = \boldsymbol{u}^p, \quad \frac{d\boldsymbol{u}^p}{dt} = \frac{1}{\mathrm{St}}(\boldsymbol{u}-\boldsymbol{u}^p), \tag{19}$$

where $\boldsymbol{x}^p$ and $\boldsymbol{u}^p$ denote the position and the velocity of a particle, respectively. The Stokes number St is the ratio between the particle relaxation time τ_p and a typical time scale of the flow. In the present paper, we define the Stokes number as

$$\mathrm{St} \equiv \frac{\tau_p \Gamma}{a^2} = \frac{2\rho_p {r_p}^2 \Gamma}{9\rho\nu a^2}, \tag{20}$$

where ρ_p and r_p denote the density and the radius of the particle, and ρ and ν denote the density and the viscosity of the carrier flow, respectively.

Transformation of Eqs. (19) to the $\boldsymbol{\xi}$-frame gives

$$\begin{aligned} \frac{d\boldsymbol{\xi}^p}{dt} &= \boldsymbol{v}^p, \\ \frac{d\boldsymbol{v}^p}{dt} &= \frac{1}{\mathrm{St}}(\boldsymbol{v}-\boldsymbol{v}^p) - \boldsymbol{\Omega}^p \times (\boldsymbol{\Omega}^p \times \boldsymbol{\xi}^p) \\ &\quad - 2\boldsymbol{\Omega}^p \times \boldsymbol{v}^p - \dot{\boldsymbol{\Omega}}^p \times \boldsymbol{\xi}^p, \end{aligned} \tag{21}$$

where $\boldsymbol{\Omega}^p$ is defined as the rotation rate due to the translation of the particle along the z-axis,

$$\boldsymbol{\Omega}^p = (0,0,\Omega^p)^T, \quad \Omega^p = \frac{a}{l} v_\zeta^p. \tag{22}$$

The three additional terms on the right-hand side of Eq. (21) represent acceleration terms due to the coordinate transformation: The centrifugal acceleration, the Coriolis acceleration, and the time-change of the rotation rate.

C. Numerical approach

The equations of motion for heavy particles, Eq. (19), combined with the equations for the flow field, Eqs. (16)–(18), are solved numerically by using a fourth order Runge-Kutta scheme. A particle trajectory is calculated for a series of decreasing values of the time step, where each next value is half of the previous value. When the differences between two subsequent trajectories are below a certain preset level, the last obtained solution is considered sufficiently accurate. For each particle, both its initial position and its initial velocity are required. The initial velocity of a particle is taken to be equal to the local velocity of the carrier flow at the position of the particle. The pipe wall is modelled as an absorbing wall; particles that reach the wall remain there.

The computation of the modified Bessel functions, which occur in the expressions of the velocity components of the carrier flow, Eqs. (16)–(18), is described in Appendix B.

III. FLOW FIELD TOPOLOGIES

We present a classification of the flow field topologies as determined by the dimensionless groups R/a, l/a, and $U_\infty a/\Gamma$. The limiting case of $R/a \to \infty$ has been described by Mezić *et al.*[13] The flow field topologies are distinguished by the presence, character, and location of stagnation points $\boldsymbol{\xi}_0$, i.e., points of zero velocity in the $\boldsymbol{\xi}$-frame,

$$v_r(\boldsymbol{\xi}_0) = \frac{1}{r}\frac{\partial \Psi}{\partial \phi} = 0, \quad v_\phi(\boldsymbol{\xi}_0) = -\frac{\partial \Psi}{\partial r} = 0. \tag{23}$$

The character of a stagnation point is fully determined by the local value of the Hessian $\mathcal{H}$, i.e., the determinant of the Hessian matrix of Ψ,

$$\begin{aligned} \mathcal{H} \equiv \left(\frac{\partial^2\Psi}{\partial\xi^2}\right)\left(\frac{\partial^2\Psi}{\partial\eta^2}\right) - \left(\frac{\partial^2\Psi}{\partial\xi\,\partial\,\eta}\right)^2 = \frac{1}{r^2}\Bigg[\left(\frac{\partial^2\Psi}{\partial r^2}\right)\left(\frac{\partial^2\Psi}{\partial\phi^2}\right) \\ + r\left(\frac{\partial\Psi}{\partial r}\right)\left(\frac{\partial^2\Psi}{\partial r^2}\right) + \frac{\partial}{\partial r}\left(\frac{1}{r}\left(\frac{\partial\Psi}{\partial\phi}\right)^2\right) - \left(\frac{\partial^2\Psi}{\partial r\,\partial\,\phi}\right)^2\Bigg], \end{aligned} \tag{24}$$

where $\xi \equiv r\cos\phi$ and $\eta \equiv r\sin\phi$. Let $\mathcal{H}_0 \equiv \mathcal{H}(\boldsymbol{\xi}_0)$, then we have the following classification:

$$\mathcal{H}_0 \begin{cases} >0 \to \text{elliptic point, extreme value of } \Psi, \\ <0 \to \text{hyperbolic point, saddle point of } \Psi. \end{cases} \tag{25}$$

Due to symmetry, stagnation points only exist on the curves $\eta=0$ and $r=\sqrt{\xi^2+\eta^2}=R/a$. On these curves $v_r \equiv 0$, and stagnation points are completely determined by the condition $v_\phi=0$. Since $\partial v_r/\partial\phi=0$ for $r=R/a$, critical points on the pipe

TABLE I. Classification of topologies in bounded space; ξ_E is the location of an elliptic point, ξ_H is the location of a hyperbolic point, and ξ_S is the location of a shear point.

Topology	No. at ξ-axis	Type and location of points at the ξ-axis	No. at pipe wall
I	0	⋯	0
II	2	$0<\xi_E<\xi_H<1$	0
III	2	$-R/a<\xi_H<\xi_E<0$	0
IV	2	$-R/a<\xi_E<0;\ 1<\xi_H<R/a$	0
V	1	$0<\xi_E<R/a$	2
VI	3	$-R/a<\xi_{E,1}<\xi_H<\xi_{E,2}<0$	2
VII	4	$-R/a<\xi_{S,1}<\xi_H<\xi_E<0;\ 1<\xi_{S,2}<R/a$	0

wall are hyperbolic points. On the ξ-axis, on the other hand, critical points can be either elliptic or hyperbolic points.

The presence of stagnation points is examined here for a wide range of values for the dimensionless parameters: $-5 \le U_\infty a/\Gamma \le 5$ (step size of 0.05), $0<l/a\le 5$ (step size of 0.05), and $R/a=1.05$, 1.1, 1.25, 1.5, 2.0, 2.5, 3.0, 4.0, 5.0, and ∞, respectively. As a result, seven different topologies occur, summarized in Table I. Examples of each topology are shown in Figs. 8(a)–8(g).

When $R/a\to\infty$, there is no wall-induced velocity, so that $U_\infty a/\Gamma$ is negative [see Eq. (A13) in Appendix A]. In this case, only topologies I, II, and III have been found, see Fig. 3. In the same figure, we also show isolines of the dimensionless vortex core thickness, ϵ/a, which is uniquely determined by the values of $U_\infty a/\Gamma$, l/a, and R/a, see Eq. (A13). The result agrees with the work of Mezic *et al.*,[13] who used different dimensionless parameters,

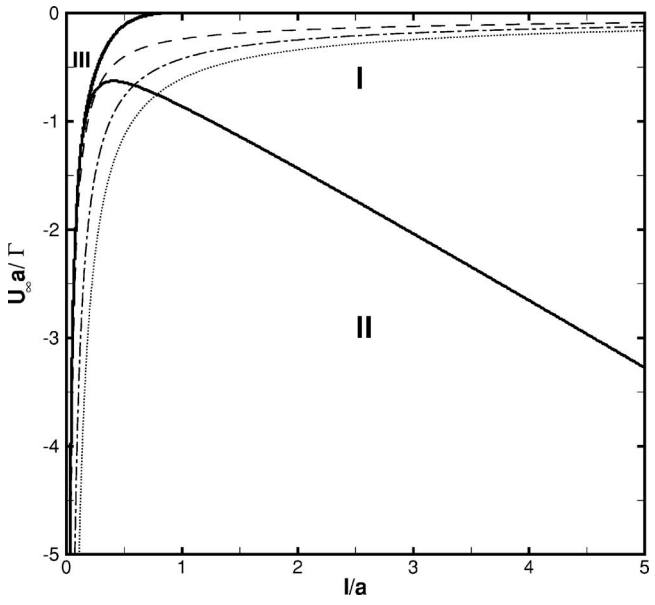

FIG. 3. Flow field topologies as a function of l/a and $U_\infty a/\Gamma$ in unbounded space ($R/a\to\infty$). Corresponding isolines of the dimensionless core radius ϵ/a are also shown; $\epsilon/a=10^{-1}$ (dashed), $\epsilon/a=10^{-2}$ (dashed-dotted), $\epsilon/a=10^{-3}$ (dotted).

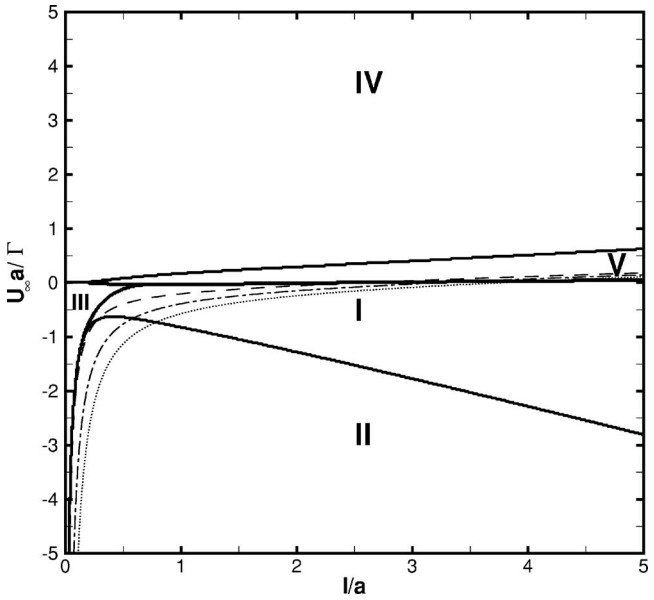

FIG. 4. Flow field topologies as a function of l/a and $U_\infty a/\Gamma$ in bounded space ($R/a=2.0$). Corresponding isolines of the dimensionless core radius ϵ/a are also shown; $\epsilon/a=10^{-1}$ (dashed), $\epsilon/a=10^{-2}$ (dashed-dotted), $\epsilon/a=10^{-3}$ (dotted).

$$a/l \quad \text{and} \quad \gamma \equiv \frac{-a}{\pi l\sqrt{1+a^2/l^2}}\left(\frac{U_\infty a}{\Gamma}\right). \tag{26}$$

Topology I is the dominant topology as the pitch l/a increases, whereas topology II occurs for a small pitch and for a moderate vortex core thickness. When $l/a>1$, topology II still exists, but then it is restricted to extremely small values of the vortex core ϵ/a. Finally, the occurrence of topology III is limited by the (l/a)-axis and the line $-U_\infty l/\Gamma=$constant.[13]

In the wall-bounded case, topologies IV, V, VI, and VII exist in addition to topologies I, II, and III. Topologies IV and V both contain one elliptic stagnation point on the nega-

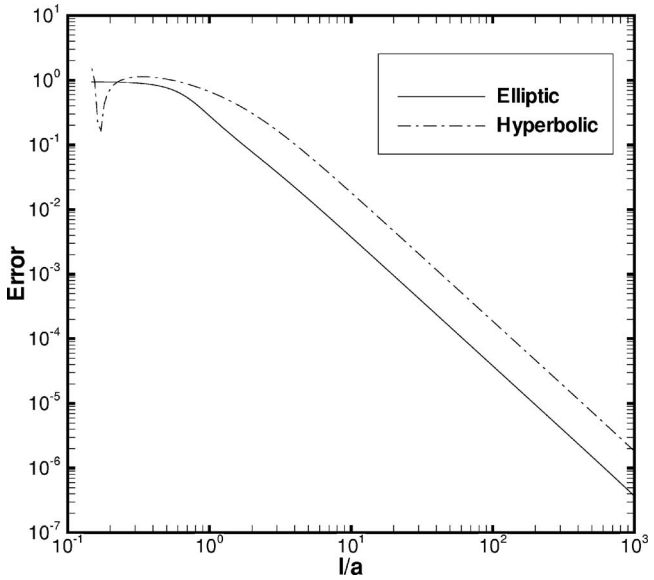

FIG. 5. Position of stagnation points in helical vortex flow field, compared to the 2D approximation, as a function of the helix pitch l/a; $R/a=2.0$.

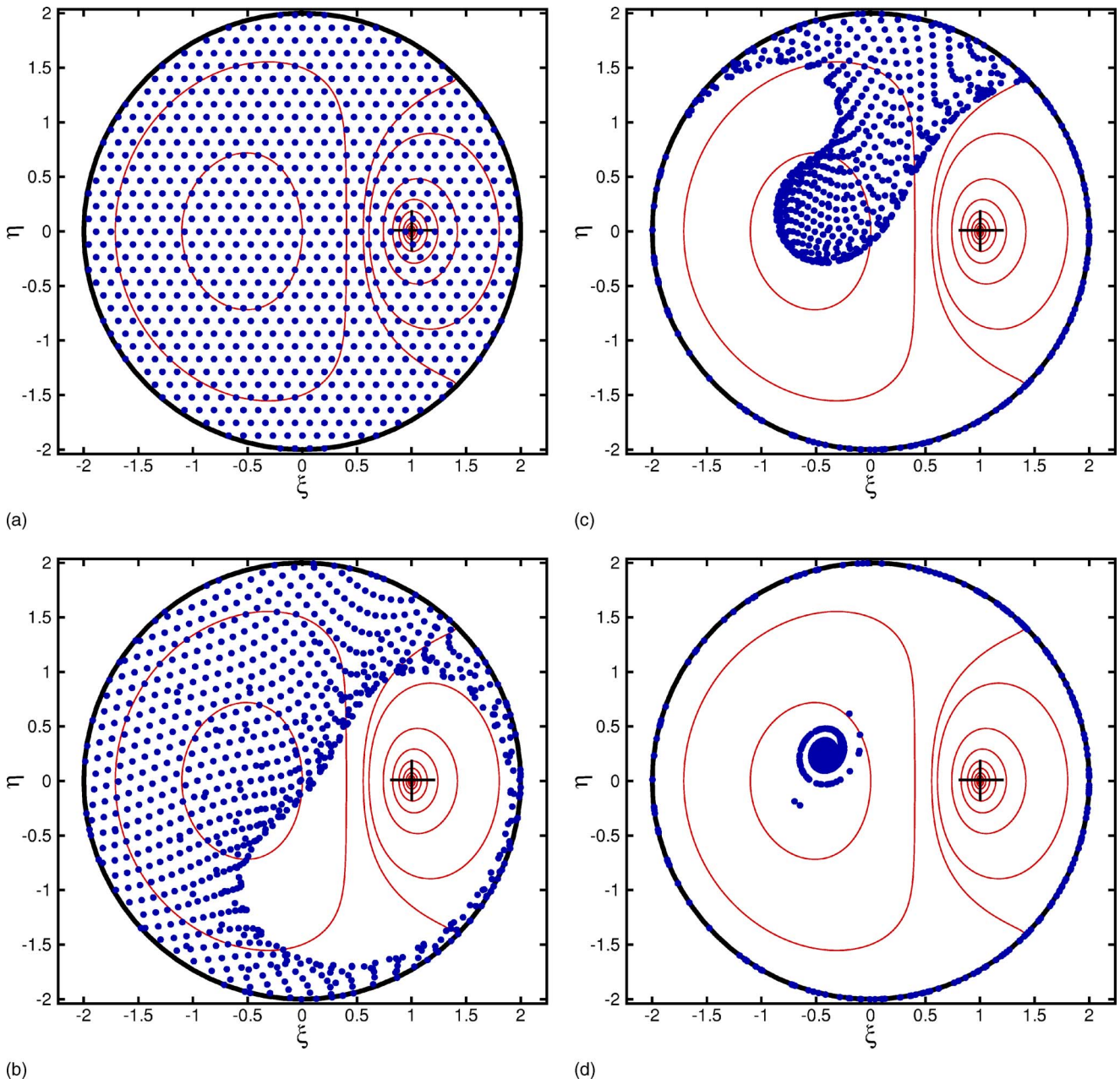

FIG. 6. (Color online) Lines: Isolines of the stream function Ψ in helical coordinates. Dots: Positions of initially uniformly distributed heavy particles in the (ξ, η)-frame in the course of time; $R/a=2.0$, $l/a=1$, $U_\infty=0.10$, St=2.0. (a) $t=0$, (b) $t=5$, and (c) $t=25$, (d) $t=100$.

tive ξ-axis, and they occur for a wide range of values for l/a, $U_\infty a/\Gamma$, and R/a. Topology VI exists in a very narrow band in parameter space only and is therefore not visible in Fig. 4. It includes two counter-rotating elliptic islands on the negative ξ-axis. Finally, topology VII occurs for very small pitches only ($l/a<0.1$), and is characterized by a circular line on which the velocity is zero; such a stagnation line corresponds to a shear flow. In Fig. 8(g), the stagnation line is denoted by the dashed circle, at $r\simeq 1.77$.

Topologies II–VII are characterized by the presence of one or two elliptic stagnation points. In topology II the elliptic stagnation point is always located on the positive ξ-axis, and the flow field around it is corotating with the vortex. In contrast, in topologies III–VII the elliptic stagnation points are all located on the negative ξ-axis, and the flow field around them is counter-rotating with the vortex.

In the limiting case of $l/a\rightarrow\infty$, topology I occurs in the unbounded case. The resulting flow field is similar to the one induced by a rectilinear vortex filament. For the wall-bounded case, topology V occurs when the helix pitch approaches infinity. This result is in agreement with the two-dimensional approximation of the helical vortex flow by a point vortex on a disk, as studied in Ref. 4. In the two-dimensional case, the self-induced velocity is zero, so that $U_\infty a/\Gamma$ is related explicitly to l/a and R/a,

$$\left(\frac{U_\infty a}{\Gamma}\right)_{2D}=\frac{l/a}{2\pi(R^2/a^2-1)}. \tag{27}$$

The influence of the torsion of the helical vortex filament

on the flow field in topology V can be assessed by comparison with the point vortex model presented in Ref. 4. We determine the position $\boldsymbol{\xi}_E$ of the elliptic stagnation point in the left half-plane and the positions $\boldsymbol{\xi}_H$ of the two hyperbolic stagnation points on the pipe wall, and compare these positions to the 2D-approximation of the flow field. The calculation is repeated for a wide range of values of the helix pitch l/a, for the case the pipe radius is taken constant at $R/a=2$. The axial velocity $U_\infty a/\Gamma$ is then obtained from Eq. (27). We define two errors as

$$\text{Error}_H = \|\boldsymbol{\xi}_{H,2D} - \boldsymbol{\xi}_{H,3D}\|,$$
$$\text{Error}_E = \|\boldsymbol{\xi}_{E,2D} - \boldsymbol{\xi}_{E,3D}\|.$$

The results are presented in Fig. 5, showing that the differences between the full 3D problem and its 2D approximation are only appreciable for $l/a \leq 10$, and vanish as $l/a \to \infty$.

IV. MOTION OF HEAVY PARTICLES

In this section we consider the motion of heavy particles in the flow fields presented in the previous section. In Fig. 6, the positions in the (ξ, η)-frame of 805 particles are plotted at four instants of time for a typical example of topology V; the particles, which have a Stokes number St=2, are uniformly distributed over the plane $z=0$ at the start of the simulation. As can be seen, some particles are quickly expelled from the circular domain. The majority of particles, however, move towards a single point at $(\xi, \eta) \simeq (-0.4, 0.2)$. This attraction point in the (ξ, η)-frame corresponds to a helical attraction trajectory in the $\boldsymbol{x}$-frame. This is illustrated by Fig. 7 where the particle positions are plotted in physical space, at four instants of time. The helical attraction trajectory is more or less in antiphase with the vortex filament.

In Fig. 8, we show the positions of initially uniformly distributed heavy particles after 100 dimensionless time units, for all topologies I–VII. Accumulation of particles in the center of the domain is observed in all topologies except for topology I. The positions of particles in physical space corresponding to Figs. 8(c) and 8(e) are plotted in Figs. 9(a) and 9(b), respectively. In Fig. 9(a), we see that a large group of particles is transported along the z-axis; these particles, which are released in the plane $z=0$ at $t=0$, are situated at $z \simeq 38$ at $t=100$. Also, Fig. 9(b) shows that many particles are concentrated on a helically shaped trajectory.

In the remainder of this section we analyze this accumulation of particles. First, it is noted that a heavy particle can only be trapped in an attraction point in the (ξ, η)-frame if two conditions are met: (1) a fixed point in the (ξ, η)-frame must exist, and (2) the fixed point must be stable. These two conditions are investigated separately.

A. Fixed points

Let (ξ^*, η^*) denote a fixed point in the (ξ, η)-frame. For a particle located at the fixed point the following relations hold:

$$\xi^p = \xi^*, \quad \eta^p = \eta^*, \quad v_\xi^p = 0, \quad v_\eta^p = 0, \quad v_\zeta^p = v_\zeta^*, \tag{28}$$

where (ξ^p, η^p, ζ^p) denotes the particle position in the $\boldsymbol{\xi}$-frame, and $(v_\xi^p, v_\eta^p, v_\zeta^p)$ denotes the corresponding particle

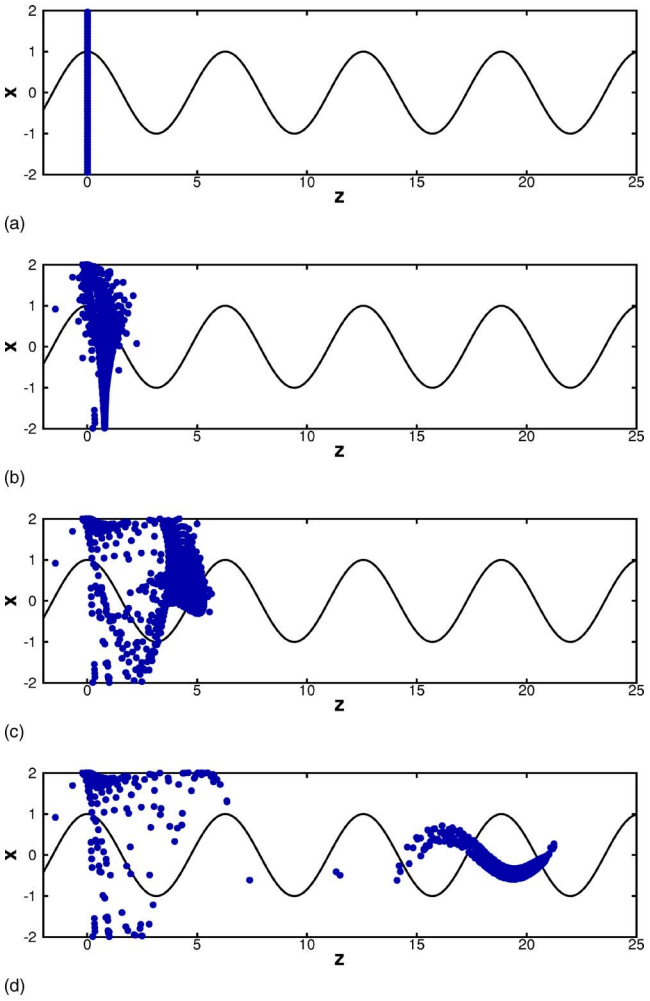

FIG. 7. (Color online) Dots: Positions of initially uniformly distributed heavy particles in physical space in the course of time; $R/a=2.0$, $l/a=1$, $U_\infty=0.10$, and St=2.0. The solid line denotes the helical vortex filament. (a) $t=0$, (b) $t=5$, (c) $t=25$, and (d) $t=100$.

velocity. Substitution of the relations (28) into the equations of motion, Eq. (21), gives

$$\begin{aligned}
&\frac{d\xi^p}{dt} = 0,\\
&\frac{d\eta^p}{dt} = 0,\\
&\frac{d\zeta^p}{dt} = v_\zeta(\xi^*, \eta^*),\\
&\frac{dv_\xi^p}{dt} = \frac{1}{St}(v_\xi(\xi^*, \eta^*)) + \Omega^{*2}\xi^* = 0,\\
&\frac{dv_\eta^p}{dt} = \frac{1}{St}(v_\eta(\xi^*, \eta^*)) + \Omega^{*2}\eta^* = 0,\\
&\frac{dv_\zeta^p}{dt} = 0,
\end{aligned} \tag{29}$$

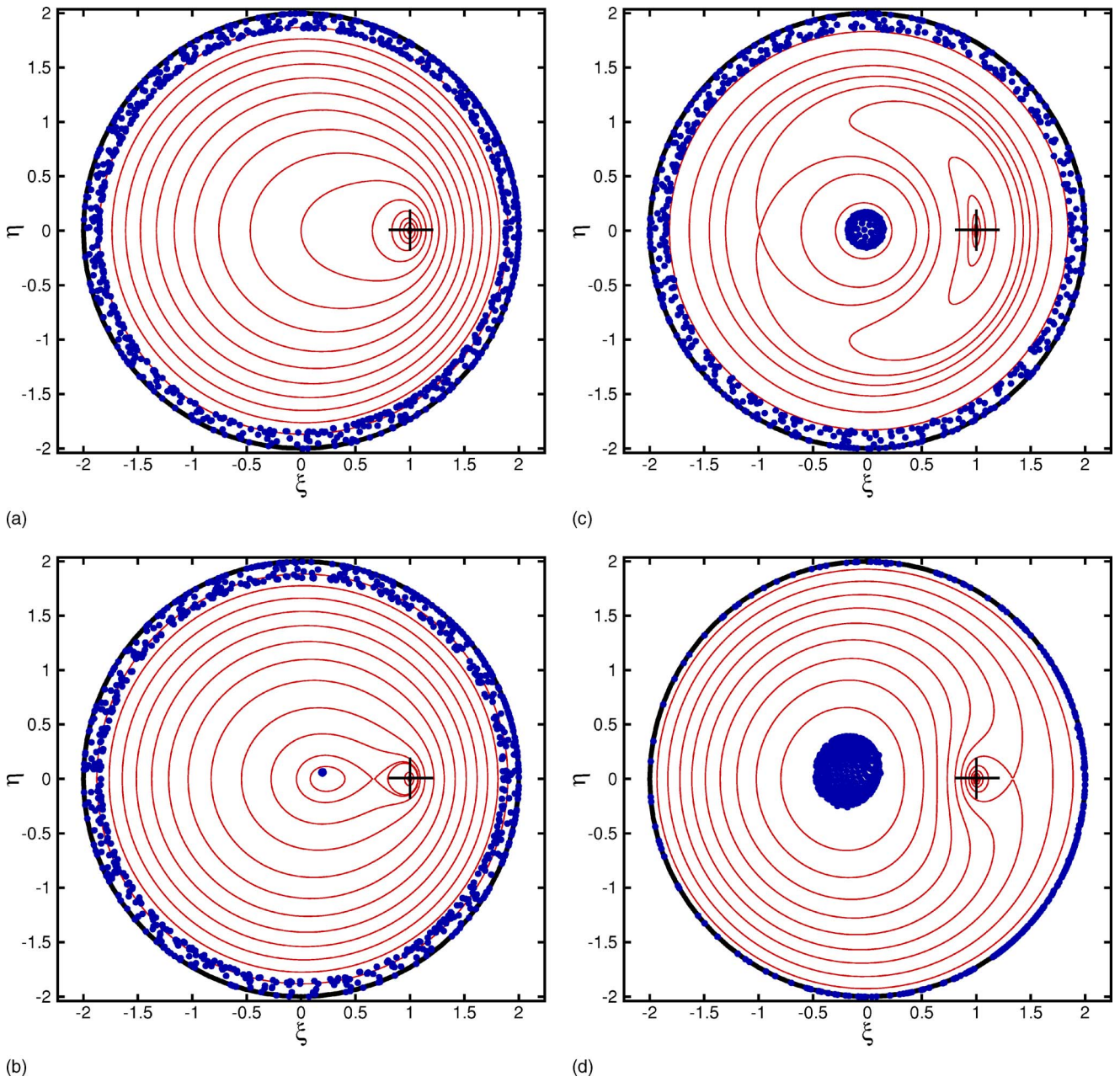

FIG. 8. (Color online) Lines: Isolines of the stream function Ψ in helical coordinates. Dots: Positions of 805 initially uniformly distributed particles with St=0.5 after dimensionless time $t=100$. (a) Topology I: $l/a=1.0$; $U_\infty a/\Gamma=-0.5$; $R/a=2.0$. (b) Topology II: $l/a=1.0$; $U_\infty a/\Gamma=-1.0$; $R/a=2.0$. (c) Topology III: $l/a=0.25$; $U_\infty a/\Gamma=-0.25$; $R/a=2.0$. (d) Topology IV: $l/a=1.0$; $U_\infty a/\Gamma=0.5$; $R/a=2.0$. (e) Topology V: $l/a=1.0$; $U_\infty a/\Gamma=0.1$; $R/a=2.0$. (f) Topology VI: $l/a=0.5$; $U_\infty a/\Gamma=-0.03$; $R/a=2.0$. (g) Topology VII (the stagnation line is indicated by a dashed line at $r\simeq 1.77$): $l/a=0.01$; $U_\infty a/\Gamma=0.0005$; $R/a=2.0$.

where $\Omega^* \equiv (a/l)v_\zeta(\xi^*, \eta^*)$. This reveals that the attraction trajectory corresponds to a point in velocity space, and to a straight line parallel to the ζ-axis in position space.

Further inspection of Eqs. (29) shows that the centrifugal force and the Stokes drag on a heavy particle are exactly balanced in a fixed point. Since the centrifugal force is always directed outward (with respect to the z-axis), we see that the velocity of the carrier flow in the fixed point must be directed in radial direction. Hence, $v_\phi=0$ and $v_r<0$. Since it can be derived from Eq. (10) that $v_r=-(1/r)\partial\Psi/\partial\phi<0$ if and only if $\eta>0$, fixed points can only occur in the upper half of the (ξ, η)-plane.

Rewriting the fourth and the fifth relation of Eq. (29) as

$$v_\xi(\xi^*, \eta^*) = -\,\mathrm{St}\,\Omega^{*2}\xi^*,$$
$$v_\eta(\xi^*, \eta^*) = -\,\mathrm{St}\,\Omega^{*2}\eta^*, \tag{30}$$

we can conclude that the fixed point for $\mathrm{St}\downarrow 0$ is located near a stagnation point in the carrier flow. A fixed point for $\mathrm{St}\to\infty$, on the other hand, satisfies $|\boldsymbol{\xi}^*|\downarrow 0$. In Fig. 10, the location of the fixed points is plotted for a range of different Stokes numbers, for topologies II and III in the unbounded case. Clearly, the fixed point for $\mathrm{St}\downarrow 0$ is the elliptic stagnation point itself, whereas the fixed point for $\mathrm{St}\to\infty$ is the origin.

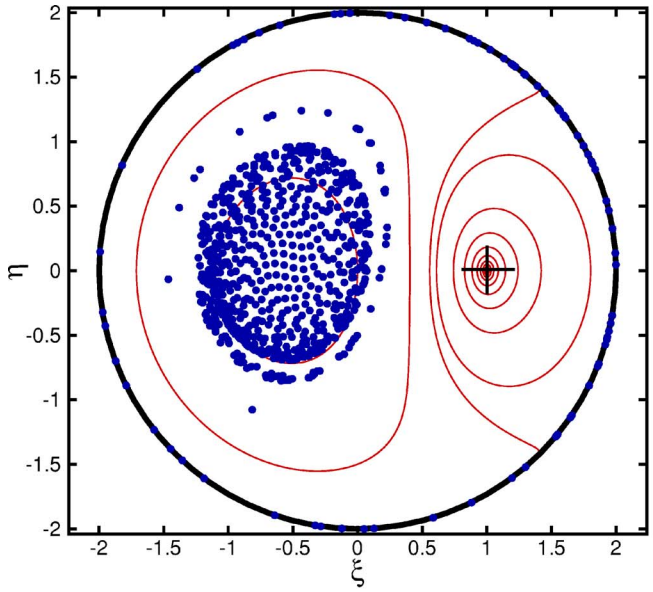

(e)

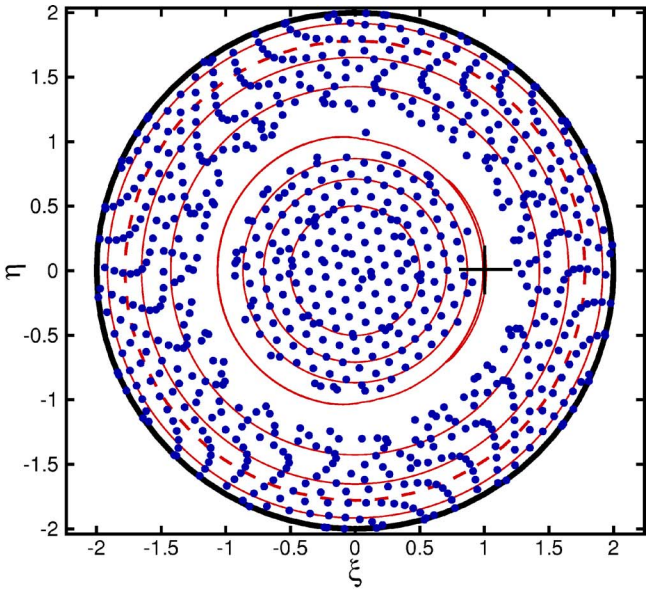

(g)

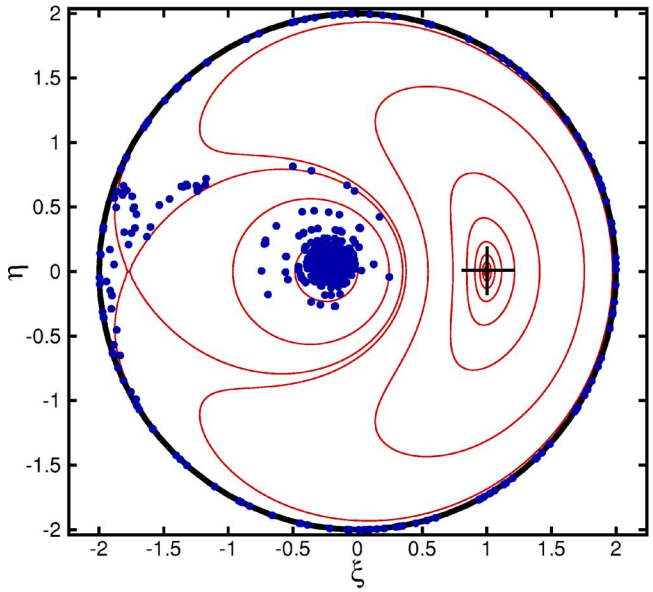

(f)

FIG. 8. (*Continued*).

B. Stability of fixed points

We investigate the stability of the fixed-point trajectories in order to determine whether they are attraction trajectories. The physical mechanism leading to particle attraction is the Coriolis force, which is directed perpendicularly to the particle trajectory in the $\boldsymbol{\xi}$-frame. When $\xi_E<0$, the flow around the elliptic stagnation point is counter-rotating with respect to the vortex, and $\Omega=(a/l)v_\zeta(\xi_E,0)>0$. As a result, the Coriolis force is directed to the center of the elliptic island. On the other hand, when $\xi_E>0$, the flow around the elliptic stagnation point is corotating with the vortex. The velocity component v_ζ, however, is negative for $\xi_E>0$, so that $\Omega<0$. Hence, also in this case the Coriolis force is directed to the center of the elliptic island. Therefore there is no qualitative distinction in particle attraction for $\xi_E>0$ (such as in topology II), compared to situations for which $\xi_E<0$ (such as in topologies III–VIII).

We carry out a linear stability analysis in order to investigate the stability of the attraction points. The five equations for ξ^p, η^p, v_ξ^p, v_η^p, and v_ζ^p in Eq. (21) are of the form

$$\frac{\mathrm{d}\boldsymbol{\chi}}{\mathrm{d}t}=\boldsymbol{f}(\boldsymbol{\chi}), \tag{31}$$

with $\boldsymbol{\chi}\equiv[\xi^p,\eta^p,v_\xi^p,v_\eta^p,v_\zeta^p]^T$. Linearization of these equations around a fixed point $\boldsymbol{\chi}^*$ leads to

$$\frac{\mathrm{d}\chi_i}{\mathrm{d}t}= f_i(\boldsymbol{\chi}^*)+(\chi_j-\chi_j^*)\frac{\partial f_i}{\partial\chi_j}\bigg|_{\boldsymbol{\chi}^*}+\mathcal{O}(|\boldsymbol{\chi}-\boldsymbol{\chi}^*|^2). \tag{32}$$

In the fixed point, $\boldsymbol{f}(\boldsymbol{\chi}^*)=0$, which reduces Eq. (32) to

$$\frac{\mathrm{d}\chi_i}{\mathrm{d}t} = \frac{\mathrm{d}(\chi_i - \chi_i^*)}{\mathrm{d}t} = (\chi_j - \chi_j^*)\frac{\partial f_i}{\partial \chi_j}\bigg|_{\boldsymbol{\chi}^*} + \mathcal{O}(|\boldsymbol{\chi}-\boldsymbol{\chi}^*|^2). \tag{33}$$

If the real parts of all eigenvalues of the matrix $\partial f_i/\partial\chi_j$ are smaller than zero, any sufficiently small perturbation in $\boldsymbol{\chi}$ with respect to $\boldsymbol{\chi}^*$ will be damped, so that $|\boldsymbol{\chi}-\boldsymbol{\chi}^*|\to 0$ as $t\to\infty$. Based on Eq. (21), the matrix $M_{ij}\equiv\partial f_i/\partial\chi_j$ is

$$M = \begin{pmatrix} 0 & 0 & \mathrm{St}^{-1}\dfrac{\partial v_\xi}{\partial\xi} + \Omega^{p2} + \eta^p\dfrac{\partial\dot{\Omega}^p}{\partial\xi} & \mathrm{St}^{-1}\dfrac{\partial v_\eta}{\partial\xi} - \dot{\Omega}^p - \xi^p\dfrac{\partial\dot{\Omega}^p}{\partial\xi} & \mathrm{St}^{-1}\dfrac{\partial v_\zeta}{\partial\xi} \\ 0 & 0 & \mathrm{St}^{-1}\dfrac{\partial v_\xi}{\partial\eta} + \dot{\Omega}^p + \eta^p\dfrac{\partial\dot{\Omega}^p}{\partial\eta} & \mathrm{St}^{-1}\dfrac{\partial v_\eta}{\partial\eta} + \Omega^{p2} + \xi^p\dfrac{\partial\dot{\Omega}^p}{\partial\eta} & \mathrm{St}^{-1}\dfrac{\partial v_\zeta}{\partial\eta} \\ 1 & 0 & -\mathrm{St}^{-1} & -2\Omega^p & 0 \\ 0 & 1 & 2\Omega^p & -\mathrm{St}^{-1} & 0 \\ 0 & 0 & \eta^p\dfrac{\partial\dot{\Omega}^p}{\partial v_\zeta^p} + 2(\Omega^p\xi^p + v_\eta^p)\dfrac{\partial\Omega^p}{\partial v_\zeta^p} & -\xi^p\dfrac{\partial\dot{\Omega}^p}{\partial v_\zeta^p} + 2(\Omega^p\eta^p - v_\xi^p)\dfrac{\partial\Omega^p}{\partial v_\zeta^p} & -\mathrm{St}^{-1} \end{pmatrix}^T. \tag{34}$$

Expressing Ω^p and $\dot{\Omega}^p$ in terms of the independent variables, and evaluating the matrix at $\boldsymbol{\chi}^*$ leads to

$$M = \begin{pmatrix} 0 & 0 & \Omega^{*2} + \mathrm{St}^{-1}\dfrac{\partial^2\Psi}{\partial\xi\,\partial\eta} + (\eta^*/\mathrm{St})(a/l)\dfrac{\partial v_\zeta}{\partial\xi} & -\mathrm{St}^{-1}\dfrac{\partial^2\Psi}{\partial\xi^2} - (\xi^*/\mathrm{St})(a/l)\dfrac{\partial v_\zeta}{\partial\xi} & \mathrm{St}^{-1}\dfrac{\partial v_\zeta}{\partial\xi} \\ 0 & 0 & \mathrm{St}^{-1}\dfrac{\partial^2\Psi}{\partial\eta^2} + (\eta^*/\mathrm{St})(a/l)\dfrac{\partial v_\zeta}{\partial\eta} & \Omega^{*2} - \mathrm{St}^{-1}\dfrac{\partial^2\Psi}{\partial\xi\,\partial\eta} - (\xi^*/\mathrm{St})(a/l)\dfrac{\partial v_\zeta}{\partial\eta} & \mathrm{St}^{-1}\dfrac{\partial v_\zeta}{\partial\eta} \\ 1 & 0 & -\mathrm{St}^{-1} & -2(a/l)v_\zeta^* & 0 \\ 0 & 1 & 2(a/l)v_\zeta^* & -\mathrm{St}^{-1} & 0 \\ 0 & 0 & -(\eta^*/\mathrm{St})(a/l) + 2\xi^*(a^2/l^2)v_\zeta^* & (\xi^*/\mathrm{St})(a/l) + 2\eta^*(a^2/l^2)v_\zeta^* & -\mathrm{St}^{-1} \end{pmatrix}^T, \tag{35}$$

where $v_\zeta^*\equiv v_\zeta(\xi^*,\eta^*)$.

1. Limit of infinite pitch

In the limit of $l/a\to\infty$, $\Omega^*\equiv(a/l)v_\zeta^*$ remains finite, and the matrix given by Eq. (35) reduces to

$$\boldsymbol{M}\big|_{l/a\gg 1} = \begin{pmatrix} 0 & 0 & 1 & 0 & 0 \\ 0 & 0 & 0 & 1 & 0 \\ \mathrm{St}^{-1}\dfrac{\partial^2\Psi}{\partial\xi\,\partial\eta} + \Omega^{*2} & \mathrm{St}^{-1}\dfrac{\partial^2\Psi}{\partial\eta^2} & -\mathrm{St}^{-1} & 2\Omega^* & 0 \\ -\mathrm{St}^{-1}\dfrac{\partial^2\Psi}{\partial\xi^2} & -\mathrm{St}^{-1}\dfrac{\partial^2\Psi}{\partial\xi\,\partial\eta} + \Omega^{*2} & -2\Omega^* & -\mathrm{St}^{-1} & 0 \\ 0 & 0 & 0 & 0 & -\mathrm{St}^{-1} \end{pmatrix}. \tag{36}$$

The characteristic polynomial for the eigenvalues λ is

$$\mathrm{St}^3\lambda^5 + 3\,\mathrm{St}^2\lambda^4 + (3\,\mathrm{St} + 2\,\mathrm{St}^3\,\Omega^{*2})\lambda^3 + (1 + 4\,\mathrm{St}^2\,\Omega^{*2})\lambda^2 + (\mathrm{St}^3\,\Omega^{*4} + 2\,\mathrm{St}\,\Omega^{*2} + \mathrm{St}\,\mathcal{H}^*)\lambda + \mathrm{St}^2\,\Omega^{*4} + \mathcal{H}^* = 0, \tag{37}$$

where $\mathcal{H}^*=\mathcal{H}(\boldsymbol{\xi}^*)$. The solution for the eigenvalues is

$$\lambda_{1,2} = \frac{-1}{2\,\mathrm{St}} + \frac{1}{2\,\mathrm{St}}\sqrt{1 - 4\,\mathrm{St}^2\,\Omega^{*2} \pm i4\,\mathrm{St}\sqrt{\mathcal{H}^*}},$$

$$\lambda_{3,4} = \frac{-1}{2\,\mathrm{St}} - \frac{1}{2\,\mathrm{St}}\sqrt{1 - 4\,\mathrm{St}^2\,\Omega^{*2} \pm i4\,\mathrm{St}\sqrt{\mathcal{H}^*}}, \tag{38}$$

$$\lambda_5 = \frac{-1}{\mathrm{St}}.$$

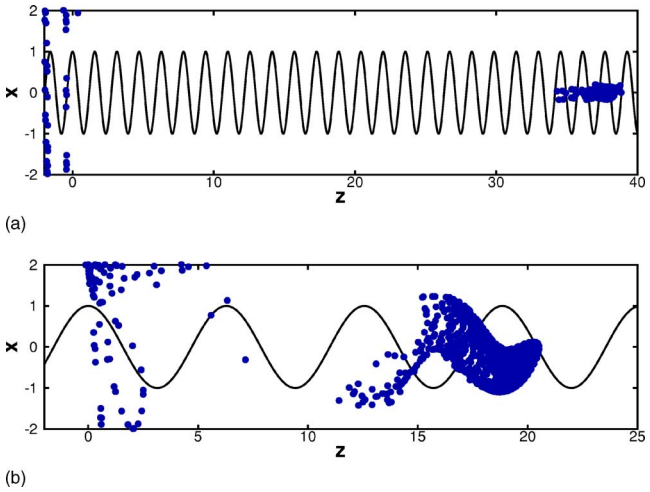

FIG. 9. (Color online) Positions of initially uniformly distributed heavy particles with St=0.5 in physical space after dimensionless time $t=100$; the solid line denotes the helical vortex filament. (a) Topology III: $l/a=0.25$; $U_\infty a/\Gamma=-0.25$; $R/a=2.0$ [corresponding to Fig. 8(c)]. (b) Topology V: $l/a=1.0$; $U_\infty a/\Gamma=0.1$; $R/a=2.0$) [corresponding to Fig. 8(e)].

For small Stokes numbers, the fixed point is located close to the elliptic stagnation point in the $\boldsymbol{\xi}$-frame, where the Hessian satisfies $0<\mathcal{H}^*<\Omega^{*2}$.[4] The eigenvalues given by Eq. (38) can then be approximated by

$$\lambda_{1,2}=-\mathrm{St}(\Omega^{*2}-\mathcal{H}^*)\pm i\sqrt{\mathcal{H}^*}+\mathcal{O}(\mathrm{St}^2),$$

$$\lambda_{3,4}=-\frac{1}{\mathrm{St}}+\mathrm{St}(\Omega^{*2}-\mathcal{H}^*)\pm i\sqrt{\mathcal{H}^*}+\mathcal{O}(\mathrm{St}^2), \tag{39}$$

$$\lambda_5=-\frac{1}{\mathrm{St}}.$$

It is observed that the real parts of all eigenvalues are negative. Hence, the fixed point is stable and it is an attraction point. The real parts of the largest eigenvalues, λ_1 and λ_2, give an indication of the attraction rate. Since it is linear in St, particle trapping occurs on a larger time scale when the Stokes number is smaller.

The above analysis is especially relevant for the wall-bounded case ($R/a<\infty$), because topology V, containing one elliptic stagnation point in the $\boldsymbol{\xi}$-frame, arises in the limit of $l/a\gg 1$. In the unbounded case ($R/a\to\infty$), however, the flow field for infinite pitch corresponds to topology I. In this topology, there are no elliptic stagnation points in the $\boldsymbol{\xi}$-frame, and therefore a stable attraction trajectory of heavy particles does not exist.

2. Limit of zero pitch

For small pitches ($l/a\downarrow 0$), we can approximate the velocity component $v_\zeta=u_z$ by Eq. (18). We note that elliptic points cannot exist for $r>1$ when $l/a\downarrow 0$. The product $I_m(mra/l)Z'_m(ma/l)$ reduces to

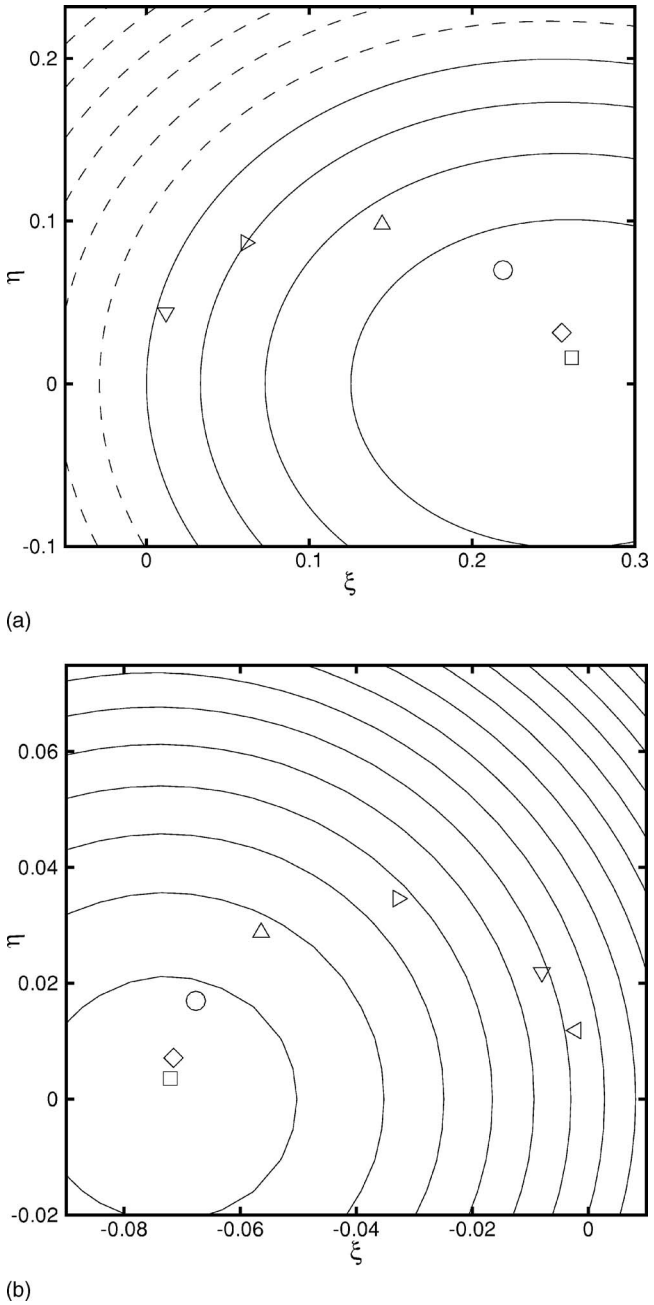

FIG. 10. Location of attraction points in two flow fields generated by a helical vortex filament, for different Stokes numbers; □ St=0.1; ◇ St=0.2; ○ St=0.5; △ St=1.0; ▷ St=2.0; ▽ St=5.0; ◁ St=10.0. (a) Topology II ($l/a=1.0$; $U_\infty a/\Gamma=-1.0$; $R/a\to\infty$). (b) Topology III ($l/a=0.25$; $U_\infty a/\Gamma=-0.50$; $R/a\to\infty$).

$$I_m(mra/l)Z'_m(ma/l)\simeq\frac{\exp[mra/l]}{\sqrt{2\pi mra/l}}\left[\frac{\pi\exp[-mra/l]}{\sqrt{2\pi ma/l}}-\frac{\pi^2\exp[mra/l-2mR/l]}{\sqrt{2\pi ma/l}}\right], \tag{40}$$

in which expansions for large arguments have been used.[29] When $l/a\downarrow 0$, the right-hand side of Eq. (40) vanishes, leading to

$$v_\zeta = \frac{U_\infty a}{\Gamma} + \mathcal{O}(l/a)^k, \quad \text{with } k \geq 1. \tag{41}$$

In addition, we know that in the limit $l/a \downarrow 0$, the velocity components in the ξ- and η-directions tend to zero inside the helix. Thus, the only possible fixed point in the rotating frame is the origin, where $\partial^2\Psi/\partial\xi^2 = \partial^2\Psi/\partial\eta^2 = \Omega^*$ and $\partial^2\Psi/\partial\xi\partial\eta = 0$. Hence, the Hessian $\mathcal{H} \rightarrow \Omega^{*2}$, and the matrix for the separation vector reduces again to the one in Eq. (36). The real parts of the eigenvalues of this matrix are $-\mathrm{St}^{-1}$ (with multiplicity 3) and 0 (with multiplicity 2), respectively, indicating that the fixed point is not an attraction point. This result is in agreement with the physical intuition that particles do not accumulate in a uniform axial jet induced by a helical vortex filament with $l/a \ll 1$, which is similar to the magnetic field induced by a spool. In conclusion, when $l/a \downarrow 0$, particle accumulation does not occur. Nevertheless, heavy particles located inside the helix, do not leave this region. In this sense, a helical vortex filament can transport heavy particles.

The flow field depicted in Fig. 8(g) is an example of a flow induced by a helical vortex filament with a very small pitch ($l/a = 0.01$). Indeed, in this configuration the particles inside the helical vortex accumulate near the origin at a slow rate, and they are transported along the z-axis with a high velocity.

3. Finite pitch

For finite values of l/a, our numerical results show that the attraction trajectory exists in all of the topologies II–VII. Particles are attracted when the Stokes number is below a critical value, which in turn depends on the values of l/a, R/a, and $U_\infty a/\Gamma$.

The attraction rate can be quantified by the first Lyapunov exponent Λ_1, defined as

$$\Lambda_1 \equiv \lim_{t\to\infty} \frac{1}{t} \ln \frac{\|\boldsymbol{\xi}_1^p(t) - \boldsymbol{\xi}_2^p(t)\|}{\|\boldsymbol{\xi}_1^p(0) - \boldsymbol{\xi}_2^p(0)\|}, \tag{42}$$

where $\boldsymbol{\xi}_1^p(t)$ and $\boldsymbol{\xi}_2^p(t)$ denote the positions of two particles, respectively, which are approaching the attraction point. When the Lyapunov exponent has a negative value, the particle trajectories converge. The convergence rate is proportional to the absolute value of the Lyapunov exponent, which depends on the dimensionless parameters.

In order to determine the dependency on the pitch, the Lyapunov exponent is calculated for a wide range of l/a. The result is plotted in Fig. 11, for two different values of $U_\infty a/\Gamma$, with $R/a = 2$ and $\mathrm{St} = 1.0$. Apparently, the Lyapunov exponent is approximately linear in $(l/a)^{-1}$. Furthermore, the Lyapunov exponent is proportional to the value of $U_\infty a/\Gamma$. This result can be explained by the observation that, when the spatial variation in v_ζ is moderate, the angular velocity of the particle in the $\boldsymbol{\xi}$-frame, Ω^p, is approximately proportional to a/l and to $U_\infty a/\Gamma$. Therefore, if either a/l or $U_\infty a/\Gamma$ increases, the Coriolis force increases, and particle accumulation is enhanced.

An interpretation in terms of the vortex core thickness ϵ/a can be given as well. From Fig. 4, it is clear that a lower value of ϵ/a corresponds to a lower value of $U_\infty a/\Gamma$ at equal l/a, or to a higher value of l/a at equal $U_\infty a/\Gamma$. Figure 11 then shows that a lower value of ϵ/a results in a lower particle accumulation rate.

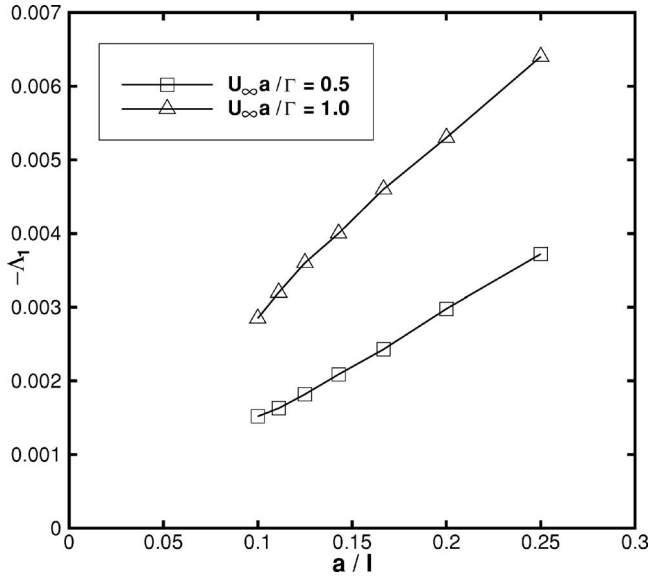

FIG. 11. The Lyapunov exponent Λ_1 as a function of the pitch l/a, for two different values of $U_\infty a/\Gamma$; $R/a = 2.0$ and $\mathrm{St} = 1.0$.

To address the dependency of the Lyapunov exponent on the particle Stokes number, we calculate Λ_1 for a range of Stokes numbers varying between 0.1 and 1.1, with $l/a = 5$, $U_\infty a/\Gamma = 0.2$ and $R/a = 2$ (topology V). The result is given in Fig. 12. It is observed that the Lyapunov exponent is approximately linear in the Stokes number in this case. This is in accordance with Eq. (37), valid for $l/a \gg 1$, which reveals that the real part of the largest eigenvalues is approximately linear in the Stokes number, as long as the Stokes number is small. In the limit of $\mathrm{St} \downarrow 0$ (passive tracer limit) there can be

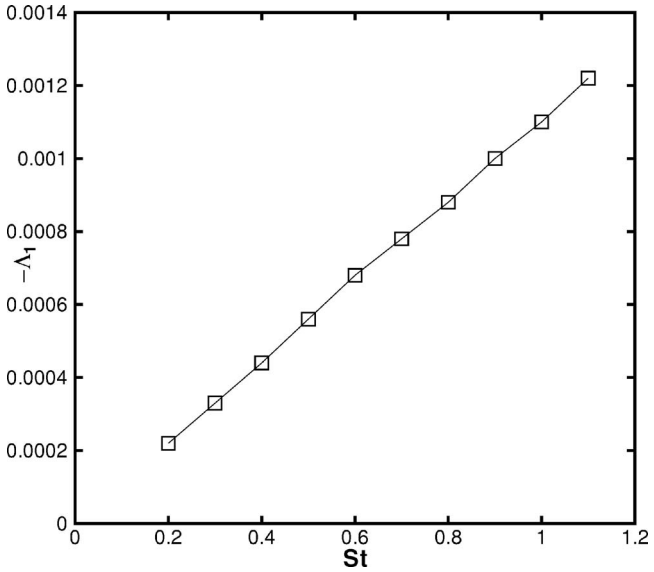

FIG. 12. The Lyapunov exponent Λ_1 as a function of the Stokes number St; $l/a = 5.0$, $U_\infty a/\Gamma = 0.2$, and $R/a = 2.0$.

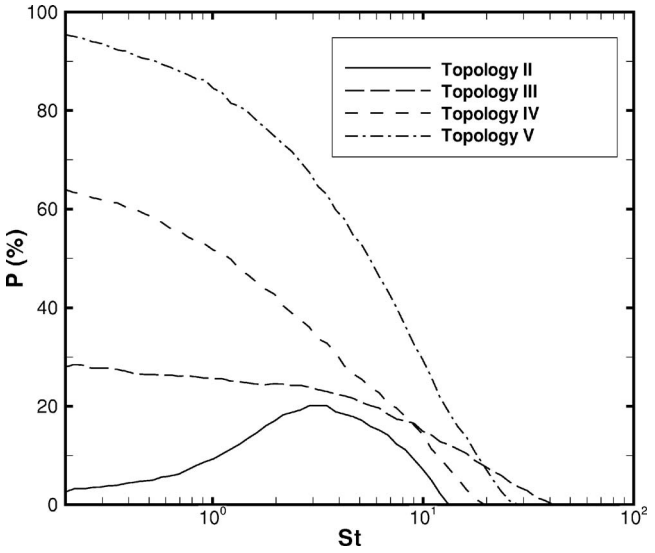

FIG. 13. Particle trapping efficiency as a function of St for topology II ($R/a=2.0$; $l/a=1.0$; $U_\infty a/\Gamma=-1.0$), topology III ($R/a=2.0$; $l/a=0.25$; $U_\infty a/\Gamma=-0.25$), topology IV ($R/a=2.0$; $l/a=1.0$; $U_\infty a/\Gamma=0.50$), and topology V ($R/a=2.0$; $l/a=1.0$; $U_\infty a/\Gamma=0.10$).

no accumulation due to continuity, so Λ_1 approaches zero. Hence, the attraction rate is proportional to the Stokes number.

It should be noted that in the limit $\mathrm{St}\to\infty$, the particle becomes insensitive to the carrier flow, and the Lyapunov exponent should go to zero. The Stokes numbers in Fig. 12, however, are not large enough to visualize this.

C. Particle trapping efficiency

The amount of particle accumulation, as function of time, can be quantified by the particle trapping efficiency P, defined as

$$P \equiv \frac{\text{number of particles with } r < R/a \text{ for } t \to \infty}{\text{total number of initially uniformly distributed particles}} \times 100\,\% . \tag{43}$$

The particle trapping efficiency, calculated on the basis of the positions of 805 initially uniformly distributed particles at time $t=1000$, is plotted in Fig. 13 as a function of the Stokes number, for typical examples of topologies I, II, III, IV, and V.

In topology I there is no accumulation at all. In topology II, P has a maximum around $\mathrm{St}=\mathcal{O}(1)$. For topologies III, IV, and V, P is close to 100% when the Stokes number is small, and close to zero when the Stokes number is large. This reflects the decreasing influence of the carrier flow on particles for increasing Stokes number.

Finally, we investigate the correlation between the particle trapping efficiency and the size of the area around an elliptic stagnation point in the (ξ,η)-plane, circumscribed by a separatrix of the stream function. The (normalized) elliptic area size is defined as

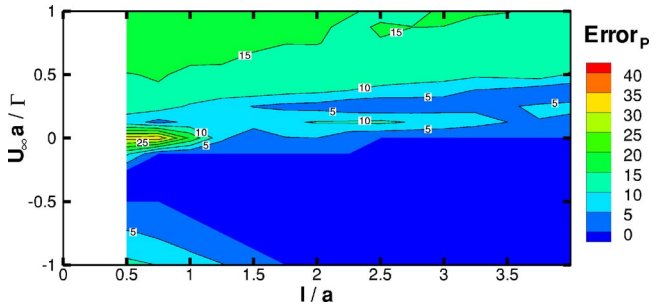

FIG. 14. (Color online) Difference between particle trapping efficiency P and the elliptic area size A_E as a function of l/a and $U_\infty a/\Gamma$; $\mathrm{St}=1.0$ and $R/a=2.0$.

$$A_E \equiv \frac{1}{\pi(R/a)^2}\int_0^{R/a}\int_0^{2\pi} H(\Psi_{\mathrm{sep}} - \Psi(r,\phi))\,r\,d\phi\,dr, \tag{44}$$

where $H(\cdots)$ is the Heaviside function and Ψ_{sep} denotes the value of Ψ at the separatrix, which is equal to the value of Ψ in the hyperbolic point on the separatrix. The correlation between A_E and P can be expressed by Error_P, defined as

$$\mathrm{Error}_P \equiv |P - A_E| \times 100\,\% . \tag{45}$$

The value of Error_P is plotted as a function of the helix pitch and the axial flow velocity in Fig. 14, for particles with $\mathrm{St}=1$, in bounded space with $R/a=2$. Clearly, the correlation between A_E and P is very good over a wide range of flow parameters. This indicates that the particle accumulation is closely related to the flow field topology in a helical vortex flow.

V. CONCLUSIONS

In the present paper, the motion of heavy particles near a helical vortex filament is investigated both numerically and analytically. The numerical simulations are based on a one-way coupling between the potential flow field and the particle equations of motion. Stokes drag is taken into account in order to isolate the effect of inertia of heavy particles on their distribution.

The numerical results reveal that heavy particles may be attracted to a helically shaped attraction trajectory. The physical mechanism leading to particle trapping is that the Coriolis force drives inertial particles to the center of an elliptic region of the stream function, where the particles are trapped by a balance between the Stokes drag and the centrifugal force.

The stability of the attraction points is proven analytically for helices with large pitch $l/a \gg 1$ in bounded space. Further analysis shows that heavy particles are captured inside the helical vortex structure when the helix pitch is small, i.e. $l/a \ll 1$. For intermediate values of the helix pitch, the particle trapping phenomenon is enhanced by the curvature and the torsion of the helical vortex, as is illustrated by the numerically determined Lyapunov exponent.

The particle accumulation is closely related to the area of an elliptic region in the stream function. These elliptic regions occur in six out of seven flow field topologies that are found.

ACKNOWLEDGMENTS

This research was carried out in Project No. TSF.6104 of the Dutch Foundation for Science and Technology (STW). Their financial and scientific support is gratefully acknowledged.

APPENDIX A: DERIVATION OF THE STREAM FUNCTION IN HELICAL COORDINATES

We derive the stream function of the velocity field in helical coordinates, Eq. (10). Although the same stream function was obtained by Alekseenko *et al.*, we propose a different derivation here.

The stream function $\Psi(r,\phi)$ can be decomposed into three terms,

$$\Psi = \Psi_u + \Psi_w + \Psi_\infty, \tag{A1}$$

where Ψ_u accounts for the flow induced by a stationary helical vortex filament in free space, Ψ_w accommodates a correction due to the presence of the pipe wall, and Ψ_∞ accounts for the uniform axial flow.

The stream function Ψ_u can be obtained from the Biot-Savart law as Hardin shows,[11]

$$\Psi_u = \begin{cases} \dfrac{1}{4\pi}\left(r^2\dfrac{a^2}{l^2}\right) - \dfrac{ra^2}{\pi l^2}\displaystyle\sum_{m=1}^{\infty} I'_m\left(\frac{ma}{l}r\right)K'_m\left(\frac{ma}{l}\right)\cos m\phi, & r<1, \\ \dfrac{1}{4\pi}\left(\dfrac{a^2}{l^2}-\ln r^2\right) - \dfrac{ra^2}{\pi l^2}\displaystyle\sum_{m=1}^{\infty} I'_m\left(\frac{ma}{l}\right)K'_m\left(\frac{ma}{l}r\right)\cos m\phi, & r>1. \end{cases} \tag{A2}$$

The stream function Ψ_w satisfies the boundary condition

$$\frac{1}{r}\frac{\partial\Psi_w}{\partial\phi} = -\frac{1}{r}\frac{\partial\Psi_u}{\partial\phi} \quad \text{for } r = R/a. \tag{A3}$$

Although an expression for Ψ_w was obtained by Okulov[15] by formally solving a partial differential equation in r and ϕ subject to the condition (A3), we present a different approach here based on the observation that Ψ_w corresponds to a continuous vortex distribution Γ'_w on the pipe wall. Because of helical symmetry, Γ'_w is a periodic function of ϕ, independent of ζ, and it can be expressed as a Fourier series,

$$\Gamma'_w(\phi') = \sum_{k=1}^{\infty}\left[a_k\cos(k\phi') + b_k\sin(k\phi')\right]. \tag{A4}$$

The coefficient a_0 has been omitted, since it only generates a uniform flow in the axial direction inside the pipe. The flow field induced follows from the Biot-Savart law, and can be calculated using Hardin's solution method (for $r<1$),

$$\begin{aligned}\Psi_w = &\int_0^{2\pi} r^2\Gamma'_w(\phi')\frac{a^2}{4\pi l^2}d\phi' \\ &- \int_0^{2\pi} r\Gamma'_w(\phi')\frac{aR}{\pi l^2}\sum_{m=1}^{\infty} I'_m(mra/l)K'_m(mR/l) \\ &\times\cos[m(\phi-\phi')]d\phi'.\end{aligned} \tag{A5}$$

With

$$\cos[m(\phi-\phi')] = \cos(m\phi)\cos(m\phi') + \sin(m\phi)\sin(m\phi'), \tag{A6}$$

and the standard integrals

$$\int_0^{2\pi}\cos(k\phi')\cos(m\phi')d\phi' = \delta_{km}\pi, \quad k,m\geq 1,$$

$$\int_0^{2\pi}\sin(k\phi')\sin(m\phi')d\phi' = \delta_{km}\pi, \quad k,m\geq 1,$$

the following expression is obtained:

$$\begin{aligned}\Psi_w = &\frac{a_0 r^2}{4}\frac{a^2}{l^2} - \frac{raR}{l^2}\sum_{m=1}^{\infty} a_m I'_m(mra/l)K'_m(mR/l)\cos(m\phi) \\ &- \frac{raR}{l^2}\sum_{m=1}^{\infty} b_m I'_m(mra/l)K'_m(mR/l)\sin(m\phi).\end{aligned} \tag{A7}$$

Substitution of Eqs. (A7) and (A2) into Eq. (A3) yields

$$a_m = -\frac{a}{\pi R}\frac{I'_m(ma/l)}{I'_m(mR/l)}, \quad m\geq 1,$$

$$b_m = 0 \quad \forall\, m.$$

and the resulting expression for Ψ_w is

$$\Psi_w = \frac{ra^2}{\pi l^2}\sum_{m=1}^{\infty} I'_m(mar/l)I'_m(ma/l)\frac{K'_m(mR/l)}{I'_m(mR/l)}\cos(m\phi). \tag{A8}$$

The stream function Ψ_∞ is computed by requiring that the helical vortex filament be stationary. Due to its curvature, the helical vortex filament induces a velocity onto itself in the binormal direction. It is well-known that the magnitude of this velocity is infinite for an infinitely thin vortex filament.[8,10,16,17] For a finite core size ϵ, however, an approximation for the self-induced velocity has been derived by Da Rios,[7]

$$\boldsymbol{U}_{s,u} = \frac{1}{4\pi(1+a^2/l^2)} \ln\left(\frac{1+l^2/a^2}{\epsilon/a}\right)\boldsymbol{b}, \tag{A9}$$

which is valid for small core radii, i.e., $\epsilon/a \ll (1+(l/a)^2)$. In addition to the self-induced motion, the vortex filament moves under the influence of the wall vorticity,

$$\boldsymbol{U}_{s,w} = \beta\left(\frac{\partial \Psi_w}{\partial r}\right)\boldsymbol{b}. \tag{A10}$$

Substitution of Eq. (A8) into Eq. (A10) yields

$$\boldsymbol{U}_{s,w} = \frac{a\sqrt{1+a^2/l^2}}{\pi l}\sum_{m=1}^{\infty} mI_m(ma/l)I'_m(ma/l)\frac{K'_m(mR/l)}{I'_m(mR/l)}\boldsymbol{b}. \tag{A11}$$

Since the product $I_m(ma/l)I'_m(ma/l)<0$, the wall-induced velocity is directed opposite to the self-induced velocity of the helical vortex filament. To obtain a stationary filament, the sum of the wall-induced velocity and the self-induced velocity must be compensated for by a uniform axial velocity U_∞, such that

$$\left(\frac{U_\infty a}{\Gamma}\boldsymbol{e}_z + \boldsymbol{U}_{s,u} + \boldsymbol{U}_{s,w}\right)\cdot \boldsymbol{b} = 0. \tag{A12}$$

Therefore,

$$\frac{U_\infty a}{\Gamma} = -\frac{1}{\pi}\frac{a}{l}\left(1+\frac{a^2}{l^2}\right)\left[\frac{1}{4}\left(1+\frac{a^2}{l^2}\right)^{-3/2}\ln\left(\frac{1+l^2/a^2}{\epsilon/a}\right) + \frac{l}{a}\sum_{m=1}^{\infty} mI_m\left(\frac{ma}{l}\right)\frac{K'_m\left(\frac{mR}{l}\right)}{I'_m\left(\frac{mR}{l}\right)}I'_m\left(\frac{ma}{l}\right)\right], \tag{A13}$$

which defines a relation between the dimensionless parameters $U_\infty a/\Gamma$, l/a, R/a, and ϵ/a. It is noted that when $U_\infty a/\Gamma>0$, wall-induced velocity dominates over self-induced velocity, and when $U_\infty a/\Gamma<0$, self-induced velocity dominates over wall-induced velocity. The corresponding stream function Ψ_∞ is

$$\Psi_\infty = \frac{r^2}{2}\left(\frac{a}{l}\right)\left(\frac{U_\infty a}{\Gamma}\right). \tag{A14}$$

Inserting Eqs. (A2), (A8), and (A14) into Eq. (A1) yields the stream function Ψ, given in Eq. (10).

APPENDIX B: COMPUTATION OF MODIFIED BESSEL FUNCTIONS

The modified Bessel functions, which occur in the equations of the flow field, Eqs. (16) and (18), are solved using a routine from Press *et al.*[28] This routine is based on a system of four equations for the unknown functions $I_n(\hat{z})$, $I'_n(\hat{z})$, $K_n(\hat{z})$, and $K'_n(\hat{z})$, for fixed n and $\hat{z}$. The algorithm is not universally applicable: For $|\hat{z}|\ll 1$, for $|\hat{z}|>10^6$, and for $n>100$, different algorithms have to be used.

First, the argument $\hat{z}$ in the modified Bessel functions becomes very small when $r\downarrow 0$, causes a problem in evaluating the term $1/rI_m(mra/l)$ which appears in Eq. (17). In order to avoid this, the following asymptotic expansion is used:[29,30]

$$I_n(\hat{z}) \simeq \frac{\left(\frac{1}{2}\hat{z}\right)^n}{n!}, \quad \text{for } \hat{z}\ll 1. \tag{B1}$$

In this way, the tangential velocity component on the z-axis becomes

$$\lim_{r\downarrow 0} u_\theta = \frac{1}{2\pi}Z'_1\left(\frac{a}{l}\right)\cos\phi. \tag{B2}$$

For large orders ($n\gg 1$), the modified Bessel functions of the first kind and their derivatives approach zero. On the other hand, the modified Bessel functions of the second kind and their derivatives approach infinity. Their products, however, remain finite. These products have been calculated using an asymptotic expansion, derived from theory of differential equations with a large parameter.[31]

Finally, for large arguments ($|\hat{z}|\to\infty$), an asymptotic expansion has been implemented, based on theory for differential equations with an irregular singularity.[31]

As was stated by Hardin,[11] the series in Eqs. (16)–(18) converge for all ϕ and $r\neq 1$. For $r=1$, the series do not converge, and for $r\simeq 1$ the convergence is very slow. Therefore, the series cannot be used if a particle is within an annular region with inner radius $r^-=1-\delta$ and outer radius $r^+=1+\delta$, with δ a small number, here taken to be equal to 0.005. Inside this shell, linear interpolation is applied

$$f(r,\phi) = \frac{(r^+-r)f(r^-,\phi)+(r-r^-)f(r^+,\phi)}{r^+-r^-}, \tag{B3}$$

for any function $f(r,\phi)$.

[1] A. K. Gupta, D. G. Lilley, and N. Syred, *Swirl Flows* (Abacus, New York, 1984).
[2] A. J. J. Verhoeff, "Aerodynamics of wind turbine rotors," Ph.D. thesis, University of Twente, The Netherlands, 2005.
[3] S. V. Alekseenko, P. A. Kuibin, V. L. Okulov, and S. I. Shtork, "Helical vortices in swirl flow," J. Fluid Mech. **382**, 195 (1999).
[4] R. H. A. IJzermans and R. Hagmeijer, "Accumulation of heavy particles in *N*-vortex flow on a disk," Phys. Fluids **18**, 063601 (2006).
[5] R. Hagmeijer, R. H. A. IJzermans, and F. Put, "Solution of the general dynamic equation along approximate fluid trajectories generated by the method of moments," Phys. Fluids **17**, 056101 (2005).
[6] L. Biferale, G. Boffetta, A. Celani, A. Lanotte, and F. Toschi, "Particle trapping in three-dimensional fully developed turbulence," Phys. Fluids **17**, 021701 (2005).
[7] L. Da Rios, "Sul moto d'un liquido indefinito con un filetto vorticoso di forma qualunque," Rend. Circ. Mat. Palermo **22**, 117 (1906).
[8] H. Levy and A. G. Forsdyke, "The steady motion and stability of a helical vortex," Proc. R. Soc. London, Ser. A **120**, 670 (1928).
[9] R. Betchov, "On the curvature and torsion of an isolated vortex filament," J. Fluid Mech. **22**, 471 (1965).
[10] D. W. Moore and P. G. Saffman, "The motion of a vortex filament with axial flow," Philos. Trans. R. Soc. London, Ser. A **272**, 403 (1972).
[11] J. C. Hardin, "The velocity field induced by a helical vortex filament," Phys. Fluids **25**, 1949 (1982).
[12] H. Lamb, "The magnetic field of a helix," Proc. Cambridge Philos. Soc. **21**, 477 (1923).

[13]I. Mezić, S. Wiggins, and A. Leonard, "Regular and chaotic particle motion near a helical vortex filament," Physica D **111**, 179 (1998).
[14]L. G. Sarasúa, A. C. Sicardi Schifino, and R. González, "The development of helical vortex filaments in a tube," Phys. Fluids **17**, 044104 (2005).
[15]V. L. Okulov, "The velocity field induced by helical vortex filaments with cylindrical or conic supporting surface," Russ. J. Eng. Thermophys. **5**, 63 (1995).
[16]G. K. Batchelor, *An Introduction to Fluid Dynamics* (Cambridge University Press, New York, 1967).
[17]R. Ricca, "The effect of torsion on the motion of a helical vortex filament," J. Fluid Mech. **273**, 241 (1990).
[18]J. Boersma and D. G. Wood, "On the self-induced motion of a helical vortex," J. Fluid Mech. **384**, 263 (1999).
[19]M. R. Maxey, "On the advection of spherical and non-spherical particles in a non-uniform flow," Philos. Trans. R. Soc. London, Ser. A **333**, 289 (1990).
[20]K. D. Squires and J. D. Eaton, "Preferential concentration of particles by turbulence," Phys. Fluids A **3**, 1169 (1990).
[21]O. A. Druzhinin, "Dynamics of concentration and vorticity modification in a cellular flow laden with solid heavy particles," Phys. Fluids **7**, 2132 (1995).
[22]A. M. Gañán-Calvo and J. C. Lasheras, "The dynamics and mixing of small spherical particles in a plane, free shear layer," Phys. Fluids A **3**, 1207 (1991).
[23]P. H. Chavanis, "Trapping of dust by coherent vortices in the solar nebula," Ann. N.Y. Acad. Sci. **356**, 1089 (2000).
[24]B. Marcu, E. Meiburg and P. K. Newton, "Dynamics of heavy particles in a Burgers vortex," Phys. Fluids **7**, 400 (1995).
[25]H. Lamb, *Hydrodynamics* (Cambridge University Press, Cambridge, 1932).
[26]M. J. Landman, "On the generation of helical waves in a circular pipe flow," Phys. Fluids A **2**, 738 (1990).
[27]M. R. Maxey and J. J. Riley, "Equation of motion for a small rigid sphere in a nonuniform flow," Phys. Fluids **26**, 883 (1983).
[28]W. C. Press, B. P. Flannery, S. A. Teukolsky, and W. T. Vetterling, *Numerical Recipes in Fortran 77* (Cambridge University Press, Cambridge, 1992).
[29]M. Abramovitz and I. A. Stegun, *Handbook of Mathematical Functions* (Dover, New York, 1964).
[30]G. N. Watson, *A Treatise on the Theory of Bessel Functions* (Cambridge University Press, Cambridge, 1966).
[31]F. W. J. Olver, *Asymptotics and Special Functions* (Academic, New York, 1974).